International Journal of Microwave and Wireless Technologies

cambridge.org/mrf

A wideband and multibeam pattern reconfigurable antenna using partially reflecting surface

Venkataswamy Suryapaga and Vikas V. Khairnar

School of Electronics Engineering, VIT-AP University, Amaravati, Andhra Pradesh 522237, India

Research Paper

Cite this article: Suryapaga V, Khairnar VV (2024) A wideband and multibeam pattern reconfigurable antenna using partially reflecting surface. *International Journal of Microwave and Wireless Technologies*, 1–9. https://doi.org/10.1017/S1759078724000941

Received: 02 May 2024
Revised: 28 August 2024
Accepted: 03 September 2024

Keywords:
high gain; multibeam pattern reconfigurable antenna; partially reflecting surface (PRS); wideband

Corresponding author: Vikas V. Khairnar; Email: vikas.vishnu@vitap.ac.in

Abstract

This paper presents a pattern reconfigurable antenna that accomplishes wideband and multibeam characteristics. The antenna design comprises a cross-slot radiator as the primary element and reconfigurable partially reflecting surface (PRS) layer placed above and below the cross-slot radiator. This configuration allows the antenna to adapt its radiation patterns effectively. The choice of the cross-slot radiator is based on its capability to offer wideband characteristics. The PRS layer consists of a precisely arranged array of 4×4 unit cells, incorporating PIN diodes into both the upper and lower PRS layers. The direction of radiation pattern can be changed by altering operating states of the PIN diodes on the PRS layer. The antenna operates in three distinct states, each exhibiting a unique radiation pattern. The antenna produces broadside, backward, and bidirectional radiation patterns. It demonstrates effective pattern reconfigurability across the frequency range of 3.10–3.86 GHz (21.71%), with a peak gain of 9.60 dBi. The simulated and measured results of the antenna are found to be in good agreement.

Introduction

Reconfigurable antennas are highly needed for modern wireless communication applications due to there several advantages such as adaptability, improved system performance, size reduction, cost savings, enhanced coverage, improved capacity, etc. [1]. Reconfigurable antennas have the capability to modify operational parameters such as frequency [2], pattern [3], and polarization [4]. In the last decade, reconfigurable antenna designs have been proposed in the literature, achieving single-parameter or multi-parameter reconfiguration [5].

Due to the mutual interaction between antenna elements, phased arrays often experience significant gain changes, particularly at lower elevation angles [6]. Pattern reconfigurable antennas need the capability to manipulate both the direction and shape of their radiation pattern to fulfill the increasing demands of future wireless communication systems. To improve signal reception and reduce interference, beam steering antennas can focus main beam of the antenna toward a particular direction. In contrast, beam shaping antennas possess the capacity to switch among various radiation patterns, encompassing omnidirectional, directional, conical, and bidirectional radiation patterns. This provides a wide range of possibilities that may be adapted to a variety of communication scenarios [7].

Pattern reconfigurable antennas with beam steering capability makes use of diverse technologies such as tunable parasitic elements [8], leaky wave antennas [9], partially reflecting surfaces (PRSs) [10], liquid metal magnetoelectric dipole [11], etc. It is important to note that the aforementioned designs are able to alter the main beam within a restricted scanning range. However, certain applications require a radiation beam that can switch between opposite directions. While there has been extensive research on the reconfiguration of radiation patterns, the exploration of multibeam capabilities has been comparatively less reported. The need for antennas capable of switching the radiation beam between opposite directions highlights a distinct challenge that may require further investigation and development in the field [12].

The design approaches used to achieve the multibeam characteristics in pattern reconfigurable antennas include dipole antennas [13, 14], monopole antenna [15], slot antennas [14, 16–19], and patch antennas with shorting pins [20, 21]. The antenna design outlined in [13] utilizes H-shaped resonator structures to attain reconfigurable patterns. This antenna can switch between the broadside and endfire patterns. It achieves a 16% impedance bandwidth, spanning from 2.47 to 2.9 GHz. This antenna has the advantage of providing high gain, a high front-to-back ratio, and a wide operational bandwidth. The pattern reconfigurable antenna design presented in [14] provides four single beams broadside, backside, endfire, and backfire. This antenna is also able to provide two bidirectional patterns. The antenna makes use of H-shaped slot with reconfigurable reflecting surfaces placed on the top and bottom side. A reconfigurable

switching network consisting of single pole three throw (SP3T) is used. A wideband pattern reconfigurable antenna, comprising a monopole as the driven element and parasitic antenna elements serving as directors is presented in [15]. This antenna is capable of generating two endfire patterns and one broadside pattern within the C band, demonstrating an overall bandwidth of 29%. The pattern reconfigurable cubic slot antenna, as proposed in [16], can switch its radiation pattern between omnidirectional and broadside radiation at an operating frequency of 2.4 GHz. This feature makes it well suited for applications in wireless sensor networks. The antenna achieves a peak gain of 2.85 dBi and 4.2 dBi, with −10 dB impedance bandwidths of 21% and 1.7% for the omnidirectional and broadside radiation, respectively. The antenna has a few limitations, including a non-planar design and varying operating bandwidths for the two operational modes. A compound reconfigurable antenna with frequency, radiation pattern, and polarization agility is discussed in [17]. This antenna is capable of producing radiation pattern in forward and backward directions. A planar antenna featuring vertical polarization, providing both omnidirectional and unidirectional pattern diversity is discussed in [18]. This antenna operates in two modes, exhibiting a 3.3% overlapping −10 dB impedance bandwidth and achieving a peak gain of 1.8 dBi. The antenna design presented in [19] is capable of adjusting its radiation pattern, half-power beamwidth, and supporting multibeam functionality. The antenna allows for seamless reconfiguration between single and multibeam radiation along the $\pm z$ direction. It exhibits a 6.18% bandwidth overlap with an average gain of 8.32 dBi. A pattern reconfigurable bidirectional antenna is explored in [20]. This antenna operates in three distinct states, offering a broadside and backward radiation pattern in state 1. In state 2, backfire and endfire radiation patterns are achieved, while state 3 yields quad-beam patterns. The antenna features a 2% overlapping −10 dB impedance bandwidth and attains a peak gain of 7.3 dBi. In [21], a circular driven patch is presented, capable of omnidirectional and endfire patterns in three distinct states. The antenna achieves a peak gain of 6.34 dBi.

Through an in-depth literature review, it is evident that there is limited coverage in the literature regarding pattern reconfigurable antennas with multibeam radiation capabilities. Certain applications specifically require antennas with the ability to produce multiple beams, indicating a gap in current research. Further investigation and development are necessary to design pattern reconfigurable antennas capable of multibeam radiation. Additionally, it has been observed that reported multibeam antennas often exhibit narrow impedance bandwidth and low gain. To address this limitation, pattern reconfigurable antennas with multibeam radiation capabilities should aim to achieve a broader range of radiation patterns, a larger operating bandwidth, high gain, a low profile, a simple design, a reduced number of active components, and efficient DC signal control circuitry.

This paper introduces a pattern reconfigurable antenna featuring a novel structure comprising a cross-slot antenna and an active PRS layer. The designed cross-slot antenna exhibits a bidirectional radiation pattern. The reconfigurable PRS layer comprises a 4×4 array of PRS unit cells loaded with PIN diodes to facilitate beam transition between different directions. Modifying states of these PIN diodes allows for the generation of broadside, backfire, and bidirectional radiation patterns. The proposed antenna achieves an overlapped fractional bandwidth of 21.83% with a peak gain of 9.60 dBi. This is achieved with a compact size of $0.81\lambda_0 \times 0.81\lambda_0 \times 0.59\lambda_0$. Rest of this paper is organized as follows: Section antenna design and working principle provides the proposed antenna design and working principle. Section results and discussion presents detailed simulated and measured results. Finally, Section conclusion concludes the paper.

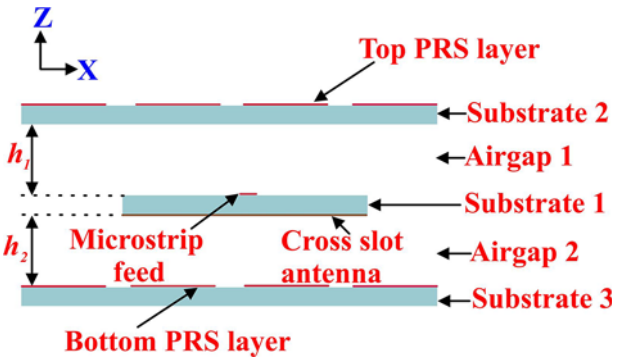

Figure 1. Cross-sectional view of the proposed antenna.

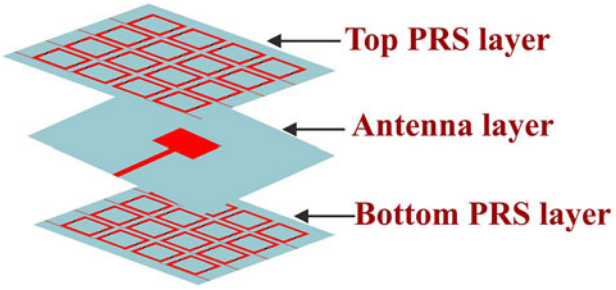

Figure 2. Isometric view of the proposed antenna.

Antenna design and working principle

The antenna design consists of three layers, incorporating a central cross-slot antenna complemented by a 4×4 active PRS unit cell array situated both at the top and bottom. This configuration is illustrated in Figs. 1 and 2. A microstrip feed is located on the upper surface of substrate 1, while a cross-slot is located on its lower surface. In addition, reconfigurable PRS layers are placed on the upper surfaces of substrate 2 and substrate 3. An air gap with a height denoted as $h_1 = 23$ mm separates the top PRS layer from the cross-slot antenna. Similarly, another air gap with a height denoted as $h_2 = 23$ mm separates the bottom PRS layer from the cross-slot antenna. In this section, we discussed the design of the unit cell, the cross-slot antenna, the PRS layer, and the working principle. To design the cross-slot antenna and PRS layer, an FR4 substrate ($\epsilon_r = 4.5$, $h = 1.6$ mm, and $\tan\delta = 0.02$) is used. The proposed antenna is simulated using Ansys High Frequency Structure Simulator (HFSS) software [22].

Unit cell

Geometrical design of the proposed unit cell is illustrated in Fig. 3. It comprises a single square loop shape with four arms, each having a PIN diode on both its left and right sides. The optimized unit cell dimensions are as follows (in millimeters): periodicity $P = 15$, inner square patch length $L_u = 10.2$, inner square patch width $W_u = 10.2$, square loop width $W_1 = 1.4$, gap between unit cells $g_1 = 2$, and gap to connect PIN diode in the square loop $g_2 = 1$.

https://doi.org/10.1017/S1759078724000941 Published online by Cambridge University Press

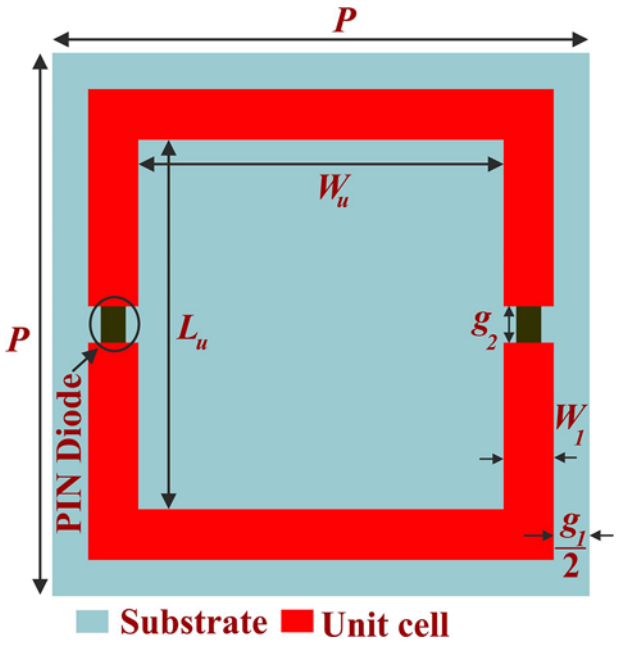

Figure 3. Geometrical design of the unit cell.

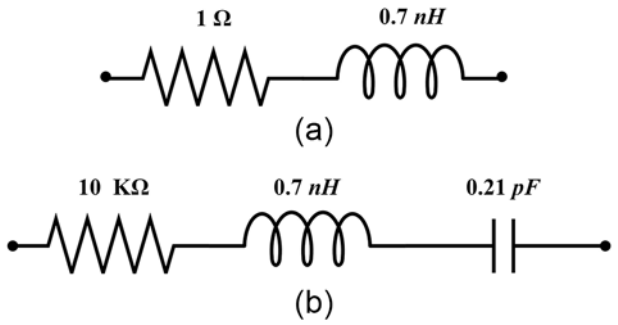

Figure 4. PIN diode equivalent circuit model (a) ON state and (b) OFF state.

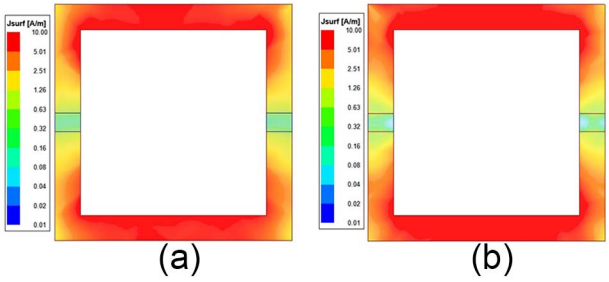

Figure 5. Simulated current distribution of the proposed unit cell (a) ON state and (b) OFF state.

Skyworks SMP1340-079LF PIN diodes, known for their fast switching speed, low capacitance, and plastic packaging are integrated into the proposed unit cell design [23]. The equivalent circuit models for the ON and OFF states of the PIN diode are displayed in Fig. 4(a) and (b) respectively. In HFSS, modeling of the PIN diodes involves considering a lumped RLC boundary. The unit cell current distributions are depicted in Fig. 5(a) and (b). In both states, the current exhibits the highest intensity along the horizontal strips of the square loop.

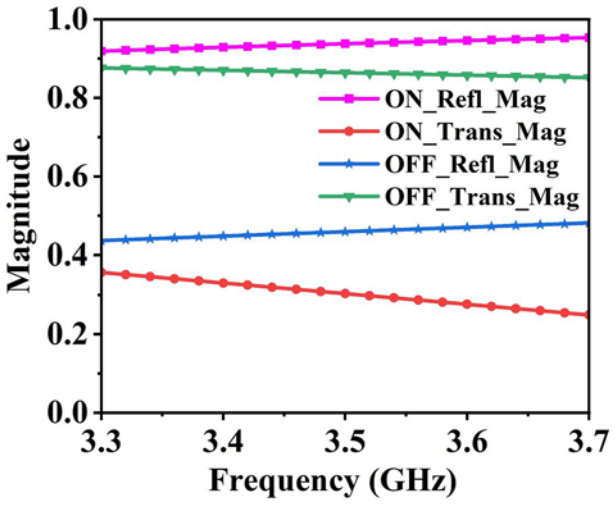

Figure 6. Simulated magnitude characteristics of the proposed unit cell.

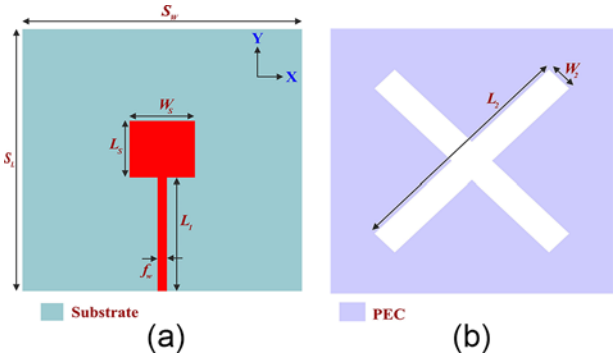

Figure 7. Cross-slot antenna. (a) Top view and (b) bottom view.

The transmission and reflection analysis of the proposed unit cell is performed using Ansys HFSS. The unit cell is simulated with periodic boundary conditions and applying Floquet ports to extract the scattering parameters, reflection coefficient $|S_{11}|$ and transmission coefficient $|S_{21}|$. The $|S_{11}|$ represents portion of the incident wave reflected back from the unit cell, while $|S_{21}|$ represents portion transmitted through the unit cell. Figure 6 shows the magnitudes of transmission and reflection for the unit cell in the PIN diode ON and OFF states. At 3.5 GHz, when the PIN diode is ON, the reflection and transmission magnitudes are 0.938 and 0.30 respectively. When the PIN diode is OFF, the reflection and transmission magnitudes are 0.459 and 0.864 respectively. Therefore, from Fig. 6, we can conclude that the unit cell acts as a reflective surface when the PIN diode is ON and as a transmissive surface when the PIN diode is OFF.

Cross-slot antenna design

The radiating element comprises a cross-slot antenna with microstrip line feeding. Figure 7(a) and (b) illustrate top and bottom views of the cross-slot antenna radiator. The proposed antenna possesses the following dimensions expressed in millimeters. The substrate dimensions include a length (S_L) of 29.5 and a width (S_W) of 29.5. The feed line dimensions consist of a length (L_1) of 14.75 and a width (f_w) of 1. The stub is defined by a length (L_S) of 6.4 and a width (W_S) of 6.9. Additionally, the cross-slot dimensions are a

https://doi.org/10.1017/S1759078724000941 Published online by Cambridge University Press

length (L_2) of 25.8 and a width (W_2) of 3, with an angle between the cross-slots set at 60°.

The PRS layer design

The PRS layer is composed of an array of 4×4 unit cells. Figure 8(a) presents the top view of this layer, while Fig. 8(b) illustrates the bottom view. The complete 4×4 PRS unit cell layer is fabricated on an FR4 substrate, with dimensions of $S_L = 70$ mm (length) and $S_W = 70$ mm (width). The PRS layer achieves reconfigurability through the incorporation of PIN diodes in unit cell. The orientation of the PIN diodes is uniform in both PRS layers. DC voltage is applied to these PIN diodes through 0.3 mm thin metallic biasing striplines on each row of unit cells. A specialized DC biasing control circuit is utilized to apply bias voltage. This unique circuitry guarantees accurate regulation of the DC voltage across the PIN diodes in the PRS layer. To simplify and optimize biasing efficiency, the grounding for all PIN diodes is strategically located on the bottom side of the PRS layer. This arrangement streamlines the biasing circuitry while maintaining effective grounding for the PIN diodes. As shown in Fig. 8(b), a via connection is utilized to connect the grounding to the top biasing lines. The purpose of adopting this arrangement is to prevent unnecessary complexity in the biasing circuitry. To mitigate the impact of RF current, 13.5 nH surface-mounted RF choke inductors are strategically incorporated within the biasing lines, aligning with established practices for minimizing RF interference [24].

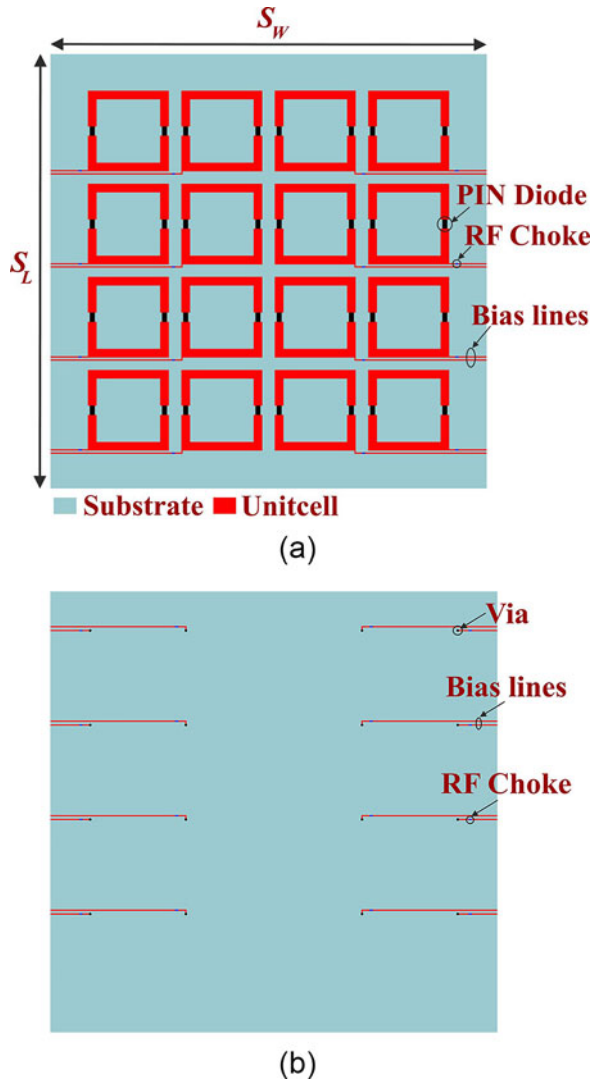

Figure 8. Active 4×4 PRS layer. (a) Top view and (b) bottom view.

Working principle

To enable pattern reconfiguration, PIN diodes are loaded on both the top and bottom PRS layer. The PRS layer generates more reflection and less transmission when its PIN diodes are ON. In contrast, more transmission and less reflection are provided by the PRS when the PIN diodes connected to this PRS layer are OFF. Table 1 presents three different operating states that are used to explain the operational concept of the proposed antenna.

In state 1, PIN diodes attached to the top PRS layer are turned OFF, while the bottom PRS layer is turned ON, resulting in a broadside radiation pattern. State 2 is the opposite of State 1, resulting in a backward radiation pattern. In state 3, there is a bidirectional radiation pattern because the PIN diodes that are connected to the top and bottom PRS layers are in the OFF state. Figure 9 shows simulated 3D polar radiation patterns at 3.5 GHz for states 1, 2, and 3.

Table 1. Operating states of the proposed antenna

State	Top PRS layer	Bottom PRS layer	Radiation pattern type
State 1	OFF	ON	Broadside
State 2	ON	OFF	Backward
State 3	OFF	OFF	Bidirectional

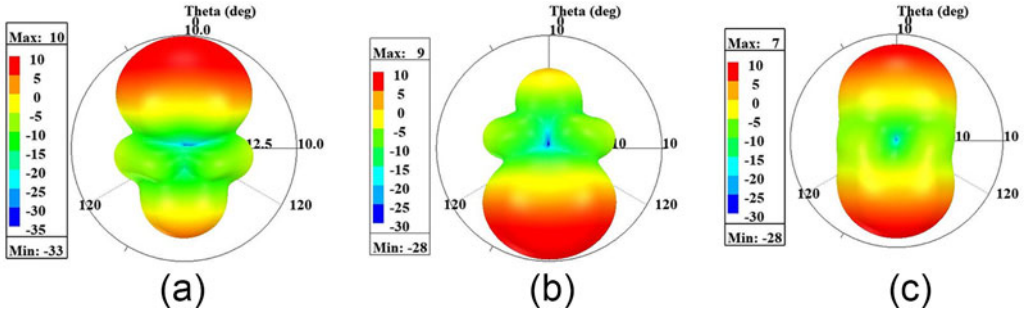

Figure 9. 3D radiation pattern at 3.5 GHz for (a) state 1, (b) state 2, and (c) state 3.

https://doi.org/10.1017/S1759078724000941 Published online by Cambridge University Press

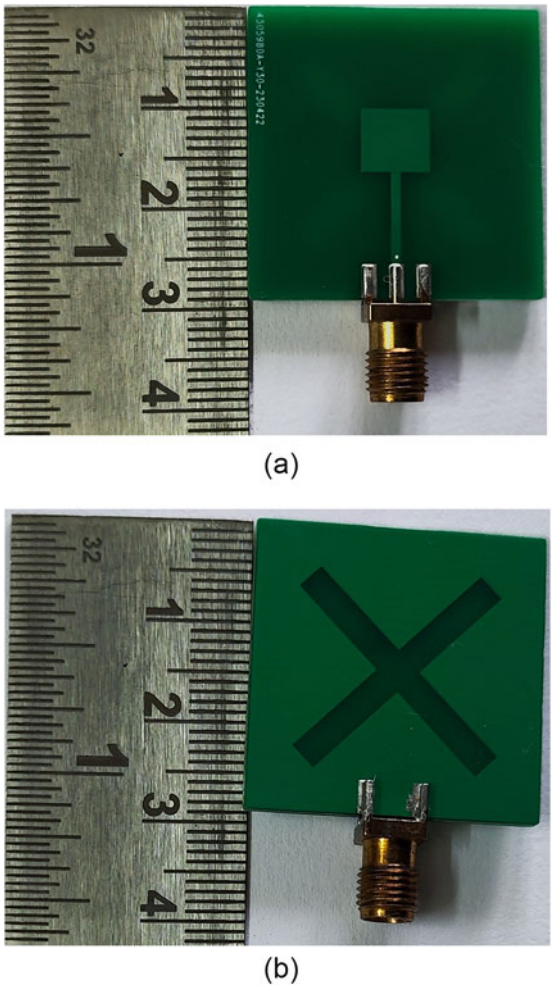

Figure 10. Fabricated prototype of the cross-slot antenna. (a) Top view and (b) bottom view.

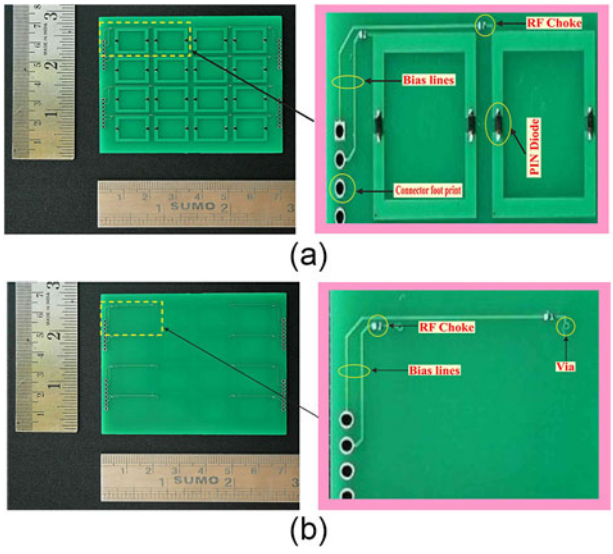

Figure 11. Fabricated prototype of the 4×4 PRS layer. (a) Top view and (b) bottom view.

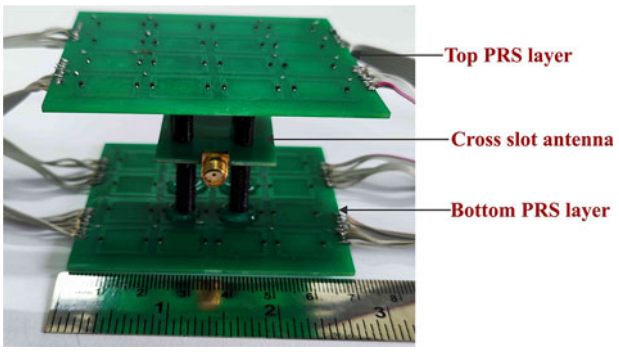

Figure 12. Fabricated cross-slot antenna with top and bottom PRS layers.

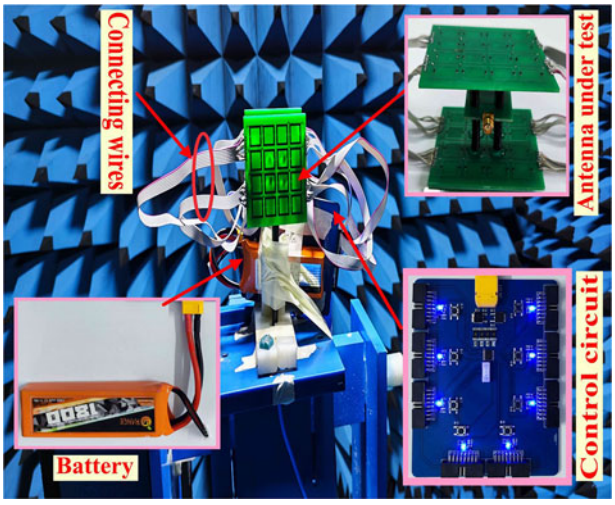

Figure 13. Antenna measurement setup in the far-field anechoic chamber.

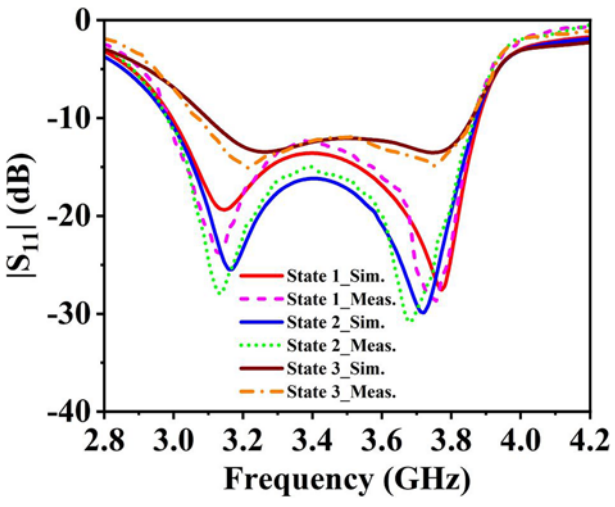

Figure 14. Simulated and measured reflection coefficient of the proposed antenna structure for state 1, state 2, and state 3.

https://doi.org/10.1017/S1759078724000941 Published online by Cambridge University Press

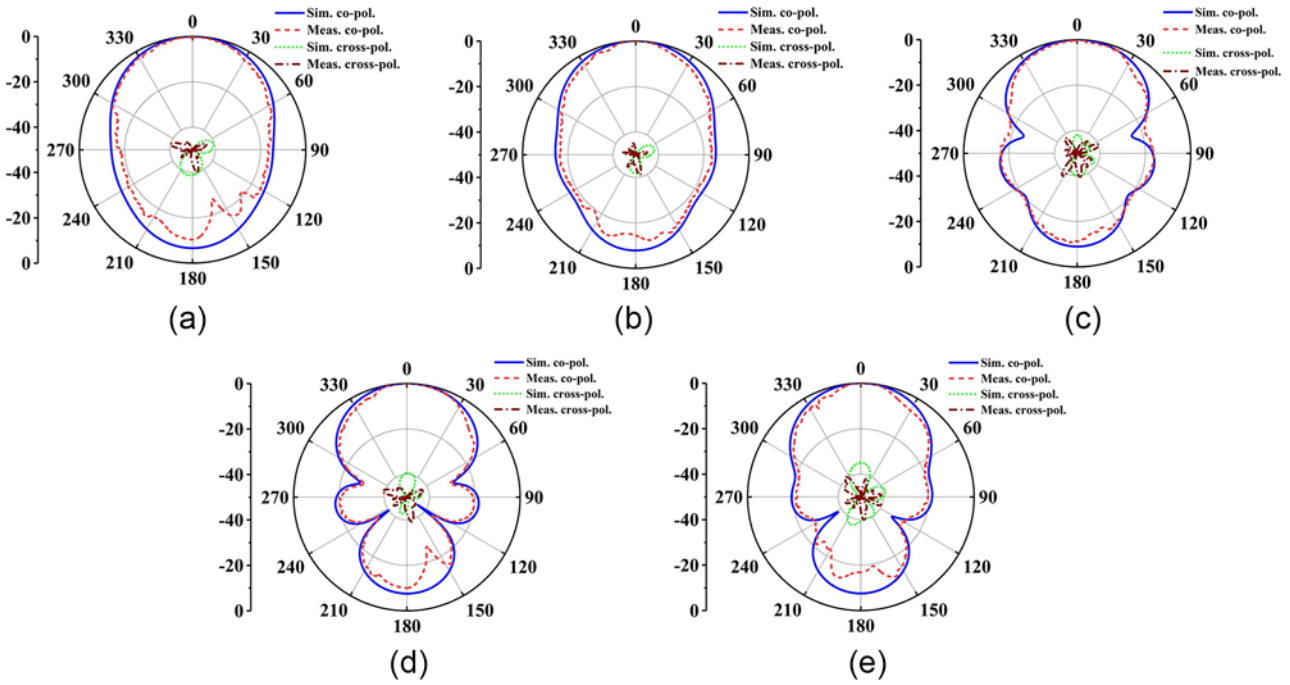

Figure 15. Simulated and measured normalized radiation patterns of state 1 in *yz*-plane (a) 3.1 GHz, (b) 3.3 GHz, (c) 3.5 GHz, (d) 3.7 GHz, and (e) 3.85 GHz.

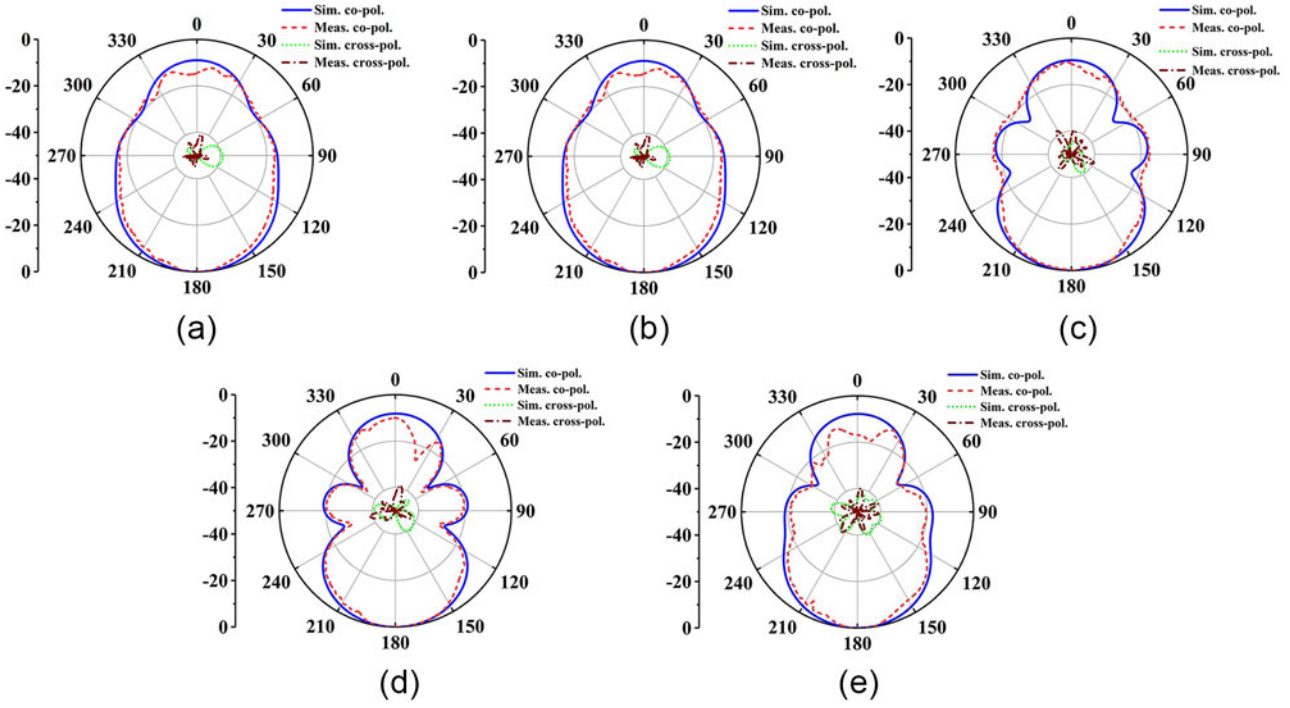

Figure 16. Simulated and measured normalized radiation patterns of state 2 in *yz*-plane (a) 3.1 GHz, (b) 3.3 GHz, (c) 3.5 GHz, (d) 3.7 GHz, and (e) 3.85 GHz.

Results and discussion

This section provides comprehensive simulated and measured results. The top view of the fabricated cross-slot antenna is shown in Fig. 10(a), while the bottom view is depicted in Fig. 10(b). Similarly, the top view of the fabricated prototype of the PRS layer is displayed in Figure 11(a), and its bottom view is presented in Fig. 11(b). Figure 12 showcases the assembled cross-slot antenna featuring both top and bottom PRS layers. The suggested antenna performance is tested in a far-field anechoic chamber, as shown in Fig. 13.

Performance of the proposed antenna has been simulated and measured in three distinct operating states. Figure 14 illustrates the simulated and measured reflection coefficients of the antenna structure for these three radiating states. In state 1, the simulated and measured −10 dB impedance bandwidth spans from 3 to 3.88 GHz, with a fractional bandwidth of 25.58%.

https://doi.org/10.1017/S1759078724000941 Published online by Cambridge University Press

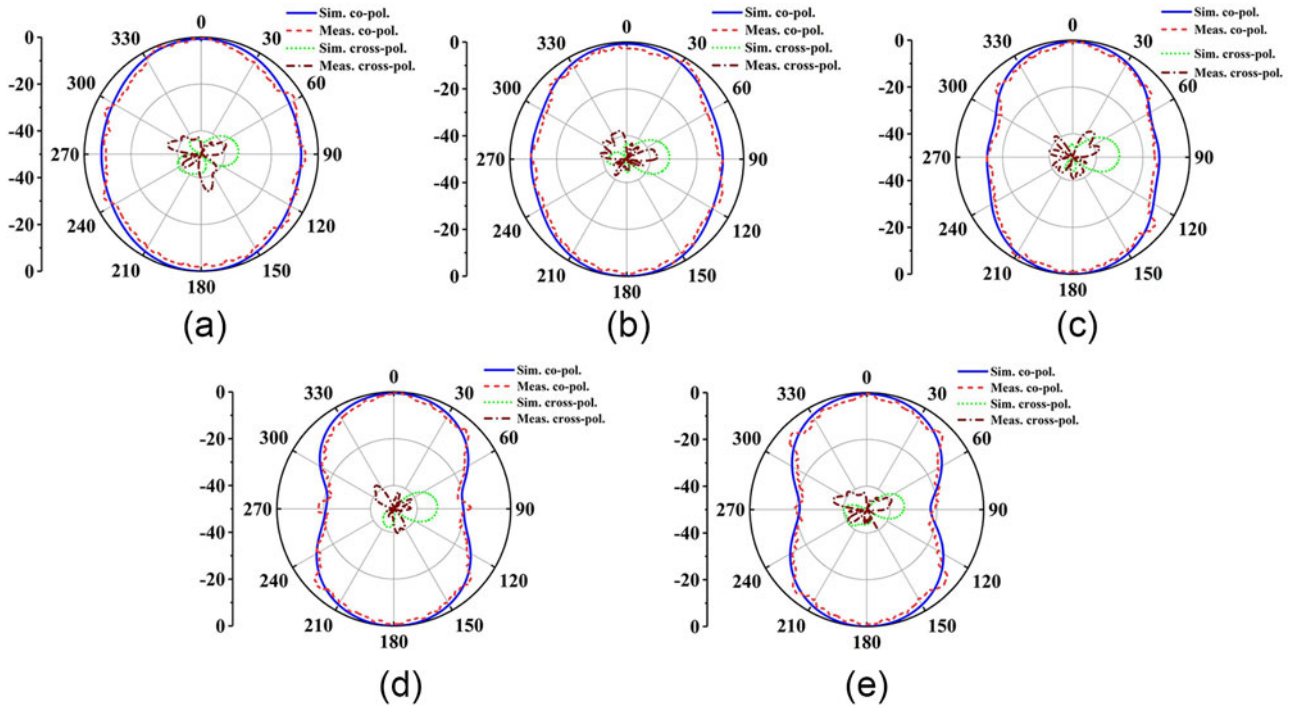

Figure 17. Simulated and measured normalized radiation patterns of state 3 in *yz*-plane (a) 3.1 GHz, (b) 3.3 GHz, (c) 3.5 GHz, (d) 3.7 GHz, and (e) 3.85 GHz.

Table 2. Performance comparison of the proposed wideband and multibeam pattern reconfigurable antenna with other reported works

Ref.	Antenna type	Operating frequency (GHz)	− 10 dB impedance bandwidth (%)	Size ($\lambda_0 \times \lambda_0 \times \lambda_0$) ($mm^3$)	Tilt direction	No. of beams	Peak gain (dBi)	Switching technique (Number)
[13]	Dipole	2.7	15.2	0.54×0.72×0.67	Broadside Endfire	2	6.4	PIN (8)
[14]	Printed dipole, slot, and RRS	2.45	8.9	0.84×0.48×0.416	Broadside Backside Endfire Backfire	4	5.8	SP3T (4)
[15]	Printed Yagi	3.5	29	1.28×0.58×0.017	Broadside Endfire	2	7.4	PIN (4)
[16]	3D folded slot antenna	2.4	2.7	0.316×0.316×0.24	Omnidirectional Broadside	2	4.2	RF switch (10)
[17]	Cavity backed slot antenna	2.31	3.5	0.86×0.78×0.01	Forward Backward	2	4	PIN (48)
[18]	Slot-loaded shorted patch	2.45	3.3	0.19×0.45×0.003	Omnidirectional Endfire	2	1.8	PIN (2)
[19]	Arcshaped slot antenna with RRS	2.45	6.18	0.98×0.37×0.41	Broadside Backward Bidirectional	3	8.32	PIN (11)
[20]	Circular shaped patch	3.4	2	2.26×2.26×0.05	Broadside Backside Endfire Backfire	4	7.3	PIN (4)
[21]	Circular shaped patch	5.8	NA	NA	Omnidirectional Endfire	2	6.34	PIN (4)
Prop.	Cross slot with PRS	3.5	21.71	0.81×0.81×0.59	Broadside Backward Bidirectional	3	9.60	PIN (64)

In state 2, the −10 dB impedance bandwidth, both simulated and measured, ranges from 2.98 to 3.87 GHz with a fractional bandwidth of 25.98%. Moving to state 3, the −10 impedance bandwidth extends from 3.10 to 3.86 GHz, as observed in both simulated and measured results with a fractional bandwidth of 21.83%.

The antenna performs multibeam switching in the *yz*-plane. Figs. 15, 16, and 17 show normalized simulated and measured radiation patterns for states 1, 2, and 3 at different frequencies. In state 1, the antenna produces broadside radiation. The achieved peak gain is 9.60 dBi with an efficiency of 84.29%. In state 2, the antenna emits backward radiation. The achieved peak gain is 9.52 dBi with

https://doi.org/10.1017/S1759078724000941 Published online by Cambridge University Press

an efficiency of 84.68%. In state 3, it emits bidirectional radiation. The achieved peak gain is 5.87 dBi with an efficiency of 84.27%. Thus, the suggested antenna performs multibeam switching, producing broadside, backward, and bidirectional radiation patterns in states 1, 2, and 3 with an overlapped bandwidth of 3.10–3.86 GHz.

Table 2 compares performance of the proposed antenna with other reported works [13–21]. The antenna introduced in [13] demonstrates two radiation patterns (broadside and endfire) across three operational states, achieving a 15.2% overlapping −10 dB impedance bandwidth and 6.4 dBi gain. In [14], the antenna offers four radiation patterns (broadside, backside, endfire, and backfire) across three states, achieving an 8.9% overlapping −10 dB impedance bandwidth and 5.8 dBi gain. Similarly, the antenna in [15] exhibits broadside and endfire patterns across three states, achieving a 29% overlapping −10 dB impedance bandwidth and 7.4 dBi gain. In [16], an antenna is presented with omnidirectional and directional patterns in two modes, featuring a 2.7% overlapping −10 dB impedance bandwidth and 4.2 dBi gain. Likewise, [17] features an antenna with forward and backward radiation patterns in two states, offering a 3.5% overlapping −10 dB impedance bandwidth and 4 dBi gain. The antenna design presented in [18] provides omnidirectional and unidirectional patterns in two modes, with a 3.3% overlapping −10 dB impedance bandwidth and a 1.8 dBi gain. In [19], multiple radiation patterns are obtained with an overall bandwidth of 6.18%. Additionally, the antenna in [20] offers broadside, backside, endfire, and backfire patterns across three states, featuring a 2% overlapping −10 dB impedance bandwidth and 7.3 dBi gain. Finally, [21] presents an antenna with omnidirectional and endfire patterns in three states, achieving a 6.34 dBi gain. It is apparent that the antennas discussed in previous studies exhibit limited −10 dB impedance bandwidth and moderate gain, which restricts their applications. In contrast, the proposed antenna demonstrates superior bandwidth and high gain, along with a compact size, making its suitability for sub-6 GHz applications.

Conclusion

A novel pattern reconfigurable antenna is presented, consisting of a wideband cross-slot antenna and a reconfigurable PRS layer. The PRS layer includes PIN diodes, which can be used to achieve different radiation patterns by changing their states. The antenna operates in three states, producing broadside, backward, and bidirectional radiation patterns. A prototype of the pattern reconfigurable antenna has been fabricated and tested. Measured results show pattern reconfigurability from 3.10 to 3.86 GHz with a peak gain of 9.60 dBi. The proposed antenna offers increased bandwidth and high gain, and its compact size enhances its suitability for sub-6 GHz applications.

Data availability statement. No data were used for the research described in the article.

Author contributions. All authors contributed equally to design and development of design, reaching conclusions, and in writing the paper.

Competing interests. The authors report no competing interests.

References

1. **Sharma SK and Chieh J-CS** (2021) *Multifunctional Antennas and Arrays for Wireless Communication Systems*. Hoboken, NJ, USA: John Wiley & Sons.
2. **Chen Z, Hao-Zhan L, Wong H, Wei H, Ren J and Yuan T** (2023) A frequency-reconfigurable dielectric resonator antenna with a water layer. *IEEE Antennas and Wireless Propagation Letters* **22**(6), 1456–1460.
3. **Yuan W, Huang J, Zhang X, Cui K, Weiwei W and Yuan N** (2023) Wideband pattern-reconfigurable antenna with switchable monopole and vivaldi modes. *IEEE Antennas and Wireless Propagation Letters* **22**(1), 199–203.
4. **Mei L, Zhang Z, Tang M-C, Zhu L and Liu N-W** (2022) Bandwidth enhancement and size reduction of a low-profile polarization-reconfigurable antenna by utilizing multiple resonances. *IEEE Transactions on Antennas and Propagation* **70**(2), 1517–1522.
5. **Khairnar VV, Ramesha CK and Gudino LJ** (2021) A parasitic antenna with independent pattern, beamwidth and polarization reconfigurability. *Wireless Personal Communications* **117**(3), 2041–2059.
6. **Khairnar VV, Kadam BV, Ramesha CK and Gudino LJ** (2018) A reconfigurable parasitic antenna with continuous beam scanning capability in H-plane. *AEU-International Journal of Electronics and Communications* **88**(May 2018), 78–86.
7. **Pablo Zapata Cano H, Zaharis ZD, Yioultsis TV, Kantartzis NV and Lazaridis PI** (2022) Pattern reconfigurable antennas at millimeter-wave frequencies: a comprehensive survey. *IEEE Access* **10**, 83029–83042.
8. **Ouyang W and Gong X** (2020) A 20-element cavity-backed slot electronically steerable parasitic array radiator (ESPAR) with 2-D beamsteering and minimized beam squint. *IEEE Antennas and Wireless Propagation Letters* **19**(8), 1420–1424.
9. **Geng Y, Wang J, Yujian L, Zheng L, Chen M and Zhang Z** (2019) Radiation pattern-reconfigurable leaky-wave antenna for fixed-frequency beam steering based on substrate-integrated waveguide. *IEEE Antennas and Wireless Propagation Letters* **18**(2), 387–391.
10. **Lu-Yang J, Zhang Z-Y and Liu N-W** (2019) A two-dimensional beam-steering partially reflective surface (PRS) antenna using a reconfigurable FSS structure. *IEEE Antennas and Wireless Propagation Letters* **18**(6), 1076–1080.
11. **Geng X, Ming S, Zhang Y, Wang A, Pan C, Chen X and Liu Z** (2022) Pattern-reconfigurable liquid metal magneto-electric dipole antenna. *IEEE Antennas and Wireless Propagation Letters* **21**(8), 1683–1687.
12. **Xuan Y, Huitema L and Wong H** (2018) Polarization and pattern reconfigurable cuboid quadrifilar helical antenna. *IEEE Transactions on Antennas and Propagation* **66**(6), 2707–2715.
13. **Ren J, Yang X, Yin J and Yin Y** (2015) A novel antenna with reconfigurable patterns using H-shaped structures. *IEEE Antennas and Wireless Propagation Letters* **14**, 915–918.
14. **Prakash T, R Kumar Chaudhary and R Kumar Gangwar** (2022) Multibeam pattern reconfigurable antenna using SP3T switching network and RRS. 2022 IEEE Microwaves, Antennas, and Propagation Conference (MAPCON). Bangalore, India: IEEE, 2037–2041.
15. **Ding X and Wang B-Z** (2013) A novel wideband antenna with reconfigurable broadside and endfire patterns. *IEEE Antennas and Wireless Propagation Letters* **12**, 995–998.
16. **Shamsinejad S, Khalid N, Monavar FM, Shamsadini S, Mirzavand R, Moradi G and Mousavi P** (2019) Pattern reconfigurable cubic slot antenna. *IEEE Access* **7**, 64401–64410.
17. **Lei G, Yujian L, Wang J and Sim C-Y-D** (2017) A low-profile reconfigurable cavity-backed slot antenna with frequency, polarization, and radiation pattern agility. *IEEE Transactions on Antennas and Propagation* **65**(5), 2182–2189.
18. **You J and Y Dong** (2023) Smart Wi-Fi antenna with reconfigurable omnidirectional and unidirectional patterns. *IEEE Antennas and Wireless Propagation Letters* **23**(3), 1010–1014.
19. **Prakash T, Kumar Chaudhary R and Kumar Gangwar R** (2024) Single/bidirectional pattern and beamwidth reconfigurable array antenna using reconfigurable reflecting surface. *Microwave and Optical Technology Letters* **66**(4), e34132.
20. **Cao S, Zhang Z, Xiaona F and Wang J** (2021) Pattern-reconfigurable bidirectional antenna design using the characteristic mode analysis. *IEEE Antennas and Wireless Propagation Letters* **20**(1), 53–57.

https://doi.org/10.1017/S1759078724000941 Published online by Cambridge University Press

21. **Lu P and Yang X-S** (2019) Pattern reconfigurable rectenna with omni-directional/directional radiation modes for MPT with multiple transmitting antennas. *IEEE Microwave and Wireless Components Letters* **29**(12), 826–829 10.1109/LMWC.2019.2943025.
22. Ansys (2021) *High Frequency Structure Simulator (HFSS)* Version 2021R1. Canonsburg, Pennsylvania, United States: ANSYS Inc.
23. Skyworks (2019) *Data Sheet of SMP1340 079L Pin DiodeS*. Irvine, California, United States: Skywork Solutions Inc.
24. Murata (2019) *Data Sheet of LQW03AW13NJ00D Wire Wound RF Inductor*. Nagaokakyo, Kyoto, Japan: Murata Manufacturing Co Ltd.

Venkataswamy Suryapaga (Student Member, IEEE) received the B.Tech degree in Electronics and Communication Engineering from Bapatla Engineering College, Bapatla, Andhra Pradesh, India in 2004 and the M.Tech. degree in Digital Electronics and Communication Systems from QIS College of Engineering, Ongole, Andhra Pradesh, India in 2010. He is currently Internal Full Time research scholar with the School of Electronics Engineering (SENSE), at VIT-AP University, Amaravati. His research interests include design of Reconfigurable Antennas using metamaterials for 5G and beyond applications.

Vikas V. Khairnar (Member, IEEE) received a B.E. degree in Electronics & Telecommunication Engineering from Savitribai Phule Pune University, India, in 2009. He obtained his M.E. in Communication Engineering from Dr. BAMU University, India, in 2013. He received the Ph.D. degree from BITS Pilani, India, in 2020. He is currently working as an Assistant Professor with the School of Electronics Engineering (SENSE), VIT-AP University, Amaravati, Andhra Pradesh, India. His research area includes the design of reconfigurable antennas, antenna arrays, and metasurface inspired antennas.

https://doi.org/10.1017/S1759078724000941 Published online by Cambridge University Press